

FLOW PHYSIC OF ACTIVE CONTROL WITH COUNTER-ROTATING CONTINUOUS JETS ON A RAMP

C. Cuvier^{1,2,4}, J.M. Foucaut^{1,2}, C. Braud^{1,3}, M. Stanislas^{1,2}
Univ Lille Nord de France¹ F-59000 Lille, EC Lille², CNRS³, ENSAM⁴,
Laboratoire de Mécanique de Lille (UMR 8107)
Boulevard Paul Langevin,
59655 Villeneuve d'Ascq Cédex, France.
christophe.cuvier@gmail.com

ABSTRACT

In this study, the flow reorganisation, given by continuous jets vortex generators (VGs) which controls the separation induced by a 22° flap on a ramp, was investigated through streamwise 2D2C PIV measurements at mid-span of the model. The VGs are set in counter-rotating arrangement. The field of view follows the wall surface. Its height is about 28.7 cm above the wall and its curvilinear length is about 94 cm, so that it contains all the separation bubble without control. Four 2k*2k cameras are used to keep a relatively good spatial resolution with this very large field. The separation is totally suppressed by the control configuration under study. The accessible Reynolds stresses with the PIV plane are presented and compared to the ones of the uncontrolled case. For the controlled flow, the three Reynolds stresses ($\overline{u'^2}$, $\overline{v'^2}$, $\overline{u'v'}$) exhibit a region of high levels which develops above the flap and which is similar to the high turbulence region which develops above the bubble border for the uncontrolled case. However, its intensity is highly reduced for the controlled flow and it is closer to the wall. The same is true for the production terms which indicates that the control applied here does not suppress totally the shear layer. It just reduces its intensity and squeezes it against the wall.

Key words : Turbulent boundary layers, 2D2C PIV, flow separation, flow control, active continuous jets.

INTRODUCTION

For turbomachinery and aircraft applications, flow separation has drastic consequences on efficiency or robustness. Controlling this phenomenon is then an important challenge. First, passive control strategies were tested (Lin (1999), Godard & Stanislas (2006a), etc.), but they were rapidly replaced by active ones due to their residual drag. The studies of Selby *et al.* (1992) and Godard & Stanislas (2006b), with basic tools for the control efficiency quantification (pressure distributions, oil-film visualisations, wall friction measurements), have brought some information about the optimum parameters of active continuous jets. More recently, with the same tools, Cuvier (2012) has completed the results of these authors on a 2D flow separation induced by a 22° flap. The incoming boundary layer thickness upstream the separation was about 19 cm and the momentum Reynolds number about 10000. For counter-

rotating continuous jets, the optimum parameters (defined in Figure 1) found are a spacing between a counter-rotating jet pair of $\frac{\lambda}{\Phi} = 27.3$, with Φ the jet diameter, a spacing between two jets of a pair of $\frac{L}{\Phi} = 15$ and a skew angle of $\alpha = 125^\circ$ (i.e. upstream blowing). The pitch angle β was fixed at 35° . For this configuration of jets, he also found that the velocity ratio VR has to be larger than 3 to reattach the flow. Finally, the smallest diameter tested (6 mm) gave the best result.

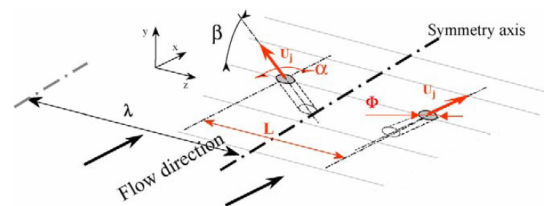


Figure 1. Counter-rotating jet parameters definition (Godard & Stanislas (2006b)).

Kostas *et al.* (2007) and Lögdberg (2008), with PIV analysis, have provided to these studies new informations about the flow modifications introduced by jet actuators. This kind of experiments are interesting to explain the active control mechanisms. Kostas *et al.* (2007) studied the flow modifications given by the Godard & Stanislas (2006b)'s optimum co and counter-rotating jet vortex generators through spanwise stereo PIV measurements at different planes downstream of the actuators. They tested both continuous and pulsed jets. Particularly, they showed the spanwise flow organisation downstream of the jets such as the approximate induced vortices position, the location of the downwash regions (i.e. where the external flow is redirected toward the wall by the vortices generated by the jets) and the upwash regions (i.e. where the flow near the wall is ejected by the induced vortices). They also provided the mean streamwise velocity and several Reynolds stresses ($\overline{u'^2}$, $\overline{v'^2}$, $\overline{w'^2}$ and $\overline{u'v'}$) profiles at different positions downstream of the actuators. Lögdberg (2008) performed in the separation region, a 2D2C PIV measurement parallel to the wall and at $y = 5$ mm from it to characterize the flow modifications generated by a counter-rotating continuous jets configuration based on the optimum generators found by Go-

August 28 - 30, 2013 Poitiers, France

dard & Stanislas (2006b). He confirmed that, downstream of the actuators, the flow at the middle of a counter-rotating jet pair corresponds to a downwash region, and the flow behind a jet to an upwash region. He also showed that the backflow in the investigated plane could be suppressed by the jets for VR larger than 1.

The present study follows the idea of the studies of Kostas *et al.* (2007) and Löfgberg (2008). It consists in characterising with a streamwise 2D2C PIV measurement, the flow modifications generated by the optimum active counter-rotating continuous jets configuration found by Cuvier (2012), which controls the flow separation induced by a 22° flap. This study gives detailed description of the turbulence organisation of the controlled flow, including some relevant turbulence production terms. The same statistics for the uncontrolled flow are also provided to highlight the modifications brought by the jets.

THE EXPERIMENT

The wind tunnel facility and the ramp

The experiments were conducted in the LML boundary layer wind tunnel at $U_\infty = 10$ m/s (see Figure 2). A boundary layer develops on the 20 m long lower wall to reach around 30 cm at the end. This thick boundary layer allows good spatial resolution. The test section is 2 m span and 1 m height and the free-stream velocity is ranging from 3 to 10 m/s ($\pm 0.5\%$). In this experiment, the wind tunnel was used in closed-loop configuration to allow temperature regulation ($\pm 0.2^\circ\text{C}$). For detailed characteristics of the wind tunnel, see Carlier & Stanislas (2005).

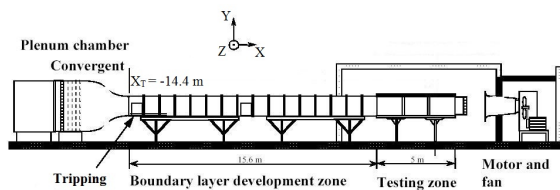


Figure 2. Schematic view of the LML wind tunnel

The ramp model was mounted on the wind tunnel floor such as the beginning of the ramp was 14.4 m downstream of the entrance of the test section. Figure 3 gives a schematic view of the ramp. It is composed of four parts. The first one is a smooth converging part with a contraction ratio of 0.75. The second part is an articulated flat plate of more than 2 m. The angle between this plate and the wind tunnel floor is called α and is counted positive if it corresponds to a positive rotation around the z axis (Figure 3). The angle α tunes the pressure gradient of the boundary layer that develops on the 2.1 m flat plate. α is ranging from 2° to -4° . The third part of the ramp is an other articulated flat plate (called flap). The angle between this plate and the wind tunnel floor is called β and its sign follows the same convention as α . β is ranging from -5° to -40° . The aim of the flap is to allow to create and fix a flow separation. The angle β tunes its strength and its extend. The last part is a flexible plate to allow smooth connection between the end of the flap and the floor of the wind tunnel.

The origin O of the wind tunnel coordinate system that will be used (see Figure 3) is placed at midspan on the lower wall, at the beginning of the converging part of the ramp.

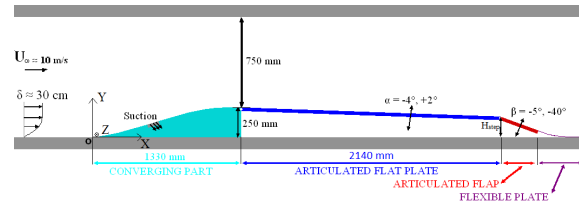


Figure 3. Schematic view of the ramp

The X-axis is along the streamwise direction, the Y-axis is normal to the wall and this reference frame is direct. In order to represent the velocity results along the ramp, a curvilinear abscissa s will be used on the model with the origin at O , and a local Frenet (x, y, z) reference frame with the origin at s , the x -axis tangent to the wall, the y -axis normal and the z -axis spanwise.

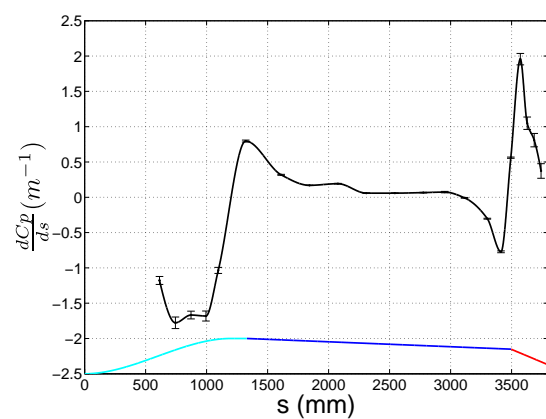


Figure 4. Streamwise pressure gradient distribution for the selected ramp configuration at $U_\infty = 10$ m/s

In the present study, the angles α and β were fixed at respectively -2° and -22° . This configuration corresponds to a mild adverse pressure gradient on the flat plate followed by a separation on the flap which remains more or less 2D. This ramp set-up was characterized with wall pressure measurements, oil-film visualisation on the flap and by 5 hot-wire profiles on the flat plate. Details about this characterization can be found in Cuvier (2012). Figure 4 gives the pressure gradient distribution along the ramp and Table 1 gives the main boundary layer parameters without control. It has to be noted that the separation starts at the flap articulation at $s = 3500$ mm.

Table 1. Boundary layer characteristics for the selected ramp configuration at $U_\infty = 10$ m/s

St	s (mm)	δ (cm)	δ^* (mm)	θ (mm)	Re_θ
St1	1508	17.4	14.4	12.2	10100
St2	1974	19.6	16.5	13.7	10600
St3	2440	20.3	17.9	14.7	11700
St4	2968	21.2	20.3	16.5	12600
St5	3382	19.0	16.4	13.5	10100

St	H	U_e (m/s)	u_τ (m/s)	$(\frac{\partial p}{\partial s})^+ (\times 10^3)$	$\beta_{Clauser}$
St1	1.18	12.9	0.482	3.28	1.44
St2	1.21	12.6	0.459	1.47	0.70
St3	1.22	12.5	0.462	0.46	0.24
St4	1.23	12.4	0.435	0.67	0.38
St5	1.21	12.3	0.465	-5.54	-2.56

The counter-rotating continuous jets

The selected counter-rotating configuration is the optimum one found by Cuvier (2012). The parameters of this configuration were given in introduction and are summarized in Table 2 (for the definition of the parameters, see Figure 1). The jets were supplied by dry compressed air through a flow rate regulation circuit which allows to tune and measure the mass flow rate at less than $\pm 2\%$ for $2 \leq q_v \leq 540 \text{ m}^3/\text{h}$. The maximum velocity difference between jets is below $\pm 2\%$ (Cuvier (2012)). In this study, VR is defined by $\frac{U_{mean}}{U_e}$, where U_{mean} refers to the mean jet velocity and U_e the local freestream velocity. The jets were set at $s = 3219 \text{ mm}$ which gives $U_e = 12.35 \text{ m/s}$ for $U_\infty = 10 \text{ m/s}$.

Table 2. Parameters of the counter-rotating jets.

Φ	$\frac{\Phi}{\delta}$	β	α	$\frac{\lambda}{\Phi}$	$\frac{L}{\Phi}$	$\frac{\Delta X_{vg}}{\Phi}$	VR
6 mm	0.03	35°	125°	27.3	15	46.8	3.5

The PIV Experiment

A streamwise 2D2C PIV set-up at mid-span of the ramp and on all the ramp flap was used in the present study (see Figure 5). This set-up is the same as the one used in Cuvier *et al.* (2013). For the controlled case, this plane is located midway between two jets of a counter-rotating pair. To obtain a large field which contains all the separation region and a part of the flow upstream and downstream of it, without scarifying the resolution, four Hamamatsu cameras of $2048 \times 2048 \text{ px}^2$ were used. Between two consecutive ones, there was a common region in order to obtain a large continuous field from the four set-ups and to obtain the uncertainty as proposed by Kostas *et al.* (2005) and Herpin *et al.* (2008). 50 mm Nikon lenses were used and the aperture was set at $f_\# = 5.6$, which gives particle image diameters about 1.3 px, which unfortunately increases the uncertainty as it is below the optimum value obtained by Foucaut *et al.* (2003). The size of the total field is about 28.7 cm in height above the wall and the curvilinear length is about 94 cm (with about 17.5 cm upstream the separation).

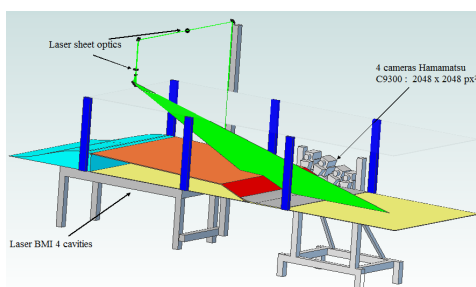


Figure 5. Scheme for the 2D2C PIV set-up used.

A light sheet of about 60 cm wide and 0.8 mm thick in the middle of the field of view was realised with a double pulsed Nd:YAG laser with an energy of 425 mJ per pulse. To minimize the laser reflection on the wall, a special rhodamine paint developed by ONERA (Office National d'études et de Recherches Aéropatiales) was applied on the ramp all along the light sheet position. The paint was

Table 3. PIV uncertainty in the merging region.

Control	region	$\frac{\Delta U}{U_\infty}$ or $\frac{\Delta V}{U_\infty}$ (%)	$\frac{\Delta u}{U_\infty}$ or $\frac{\Delta v}{U_\infty}$ (%)	random error (px)
none	Outer flow	1	0.8	0.11 - 0.23
	Near wall	4	3	0.28
counter	Outer flow	1.5	2	0.13 - 0.45
	Near wall	3.5	4	0.85

applied on a 2 cm wide and 0.18 mm thick black electrical insulation tape to easily renew it. The total thickness of the tape and the rhodamine paint was about 0.25 mm, which corresponds to about 8 wall units before the separation. To filter the rhodamine emission, bandpass filters, centred at the laser wave length, were set on the 50 mm Nikon lenses. The time between the two laser pulses was set at $\Delta t = 80 \mu\text{s}$, so that the out of plane motion was limited, as recommended by Foucaut *et al.* (2003). The free-stream displacements is then of the order of 6 to 7 pixels, which does not optimize the dynamic, as near the recirculation bubble and the wall the velocities are largely smaller.

To obtain the velocity in the local reference frame attached to the wall, special software were made to make a special PIV mesh which follows the wall (i.e. each vertical mesh line is normal to the local surface). The meshing procedure is explained in Cuvier (2012). The meshes size used was $10 \times 10 \text{ pixels}^2$ (for $32 \times 32 \text{ px}^2$ interrogation windows, the mean overlapping is about 70%, maximum 90% and minimum 35%). The distance from the wall of the first mesh point was 16 pixels to prevent laser reflection to be inside the interrogation windows. The grid has 642 points along the wall and 188 points along the wall-normal direction. This leads to a mean grid spacing of $1.5 \text{ mm} \times 1.5 \text{ mm}$. This corresponds to about 45 wall units, with u_τ taken at $s = 3382 \text{ mm}$ and without flow control. The first measurement point is at 2.4 mm from the wall which corresponds to about 72 wall units.

The MatPIV.1.6.1 toolbox for Matlab software, written by J. K. Sveen from Oslo University, was modified and used under the free software Octave. Four passes were used, a first one with $64 \times 64 \text{ px}^2$ interrogation window and three with $32 \times 32 \text{ px}^2$. In the final pass, the software used a 1D Gaussian fit based on three points to obtain displacement accuracy below 1 px.

For the present experiment, 5000 uncorrelated fields at 4 Hz were acquired for the controlled and uncontrolled flow to obtain a convergence on the mean value below $\pm 1\%$ and on the turbulence intensity below $\pm 4\%$. The uncertainties estimated in the merging regions are summarized in Table 3 (for more details about these uncertainties estimation see Cuvier (2012) and Cuvier *et al.* (2013)). When there is two values in the column, the first one refers to the upstream part of the flow and the second one to the downstream part. u refers to $\sqrt{u'^2}$ and v to $\sqrt{v'^2}$. For the controlled flow, the uncertainties increase. This is due to stronger out of plane motion generated by the jets which develops with the streamwise position. The uncertainty on the mean velocity and on the turbulent intensity remain however acceptable to draw conclusions.

RESULTS

Mean velocity and separation

In order to obtain a better assessment of the near wall flow behaviour, the velocities will be represented only in the local reference frame attached to the wall (x, y, z). U is

August 28 - 30, 2013 Poitiers, France

the velocity parallel to the wall and V the velocity normal to it. Figure 6 shows the mean streamwise velocity distribution normalized by $U_\infty = 10 \text{ m/s}$ for the uncontrolled and controlled flow. Before the flap corner, higher velocities are observed near the wall for the controlled flow (Figure 6 b)). As the measurement plane is located midway between two jets of a counter-rotating jet pair, this is an agreement with a downwash region as shown by Godard & Stanislas (2006b), Kostas *et al.* (2007), Lögdberg (2008), etc.. The acceleration at the corner is more extended and connected to the outer flow. Over the flap, the flow is apparently fully reattached (no separation is detected by the $\chi = 50\%$ criterion of Simpson (1989), completed by a linear extrapolation of this coefficient at the wall based on the studies of Dengel & Fernholz (1990) and Lögdberg *et al.* (2010), if the two first points present a χ greater than 0.3). This agrees with previous measurements of the skewness given by a friction probe located near $X = 3.71 \text{ m}$ (Cuvier (2012)). The shear layer is closer to the wall and the region of velocity deficit is significantly reduced at the outlet compared to the uncontrolled case.

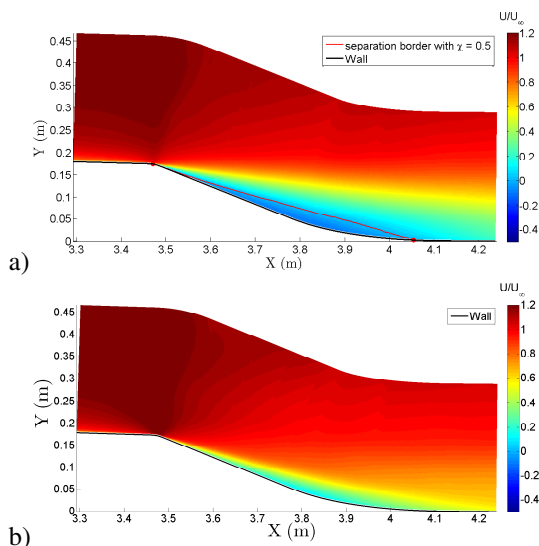


Figure 6. Mean streamwise velocity U on the flap for a) the uncontrolled, b) the controlled flow.

Turbulence Intensities

Streamwise turbulence intensity

Figure 7 shows for the uncontrolled and controlled flow, the streamwise turbulence intensity distribution $u = \sqrt{u'^2}$ on the flap normalized by U_∞ . The same color scale is used to facilitate the comparisons. For the controlled case (Figure 7 b)), the merging regions appear as discontinuities in the figure because larger errors are observed compared to the uncontrolled case (see Table 3) due mostly to a stronger out of plane component. As in these regions, the velocity is set by a mean of the two values obtained, this decreases the random PIV uncertainty, so the positive bias on the turbulence intensity. This explains why in the merging regions, the turbulence intensity is lower than on both sides of them. It will be the case for all the following figures which present turbulent quantities for the controlled case.

For the actuated configuration (Figure 7 b)), upstream

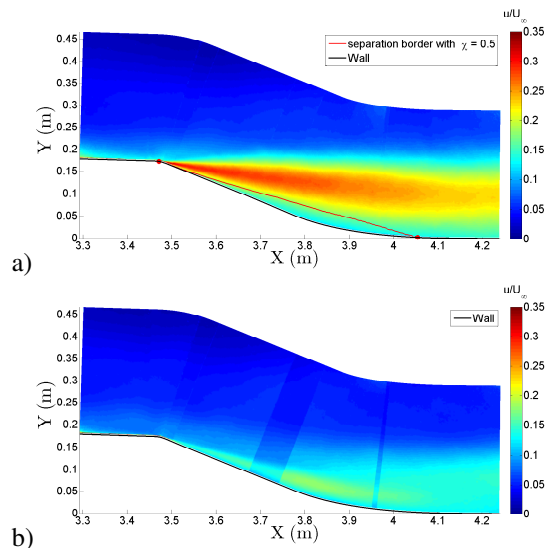


Figure 7. Streamwise turbulence intensity ($u = \sqrt{u'^2}$) on the flap for a) the uncontrolled, b) the controlled flow.

of the flap, in the near wall region, lower values are observed compared to the uncontrolled case (Figure 7 a)). This agrees with the downwash region which attenuates turbulence near the wall due to the low turbulence external flow entrained toward the wall. After the flap corner, a significant change is observed. Much lower values appear near the wall compared to the uncontrolled flow, even if a region of high values is also observed much closer to the wall in the downstream part. The turbulence level in this region is however two times lower than for the uncontrolled flow. The lower streamwise turbulence intensity value on the flap could be explained by the disappearance or reduction in size of the large scale structures characterized by high u' fluctuations observed for the uncontrolled flow (Cuvier (2012), Cuvier *et al.* (2013)).

Wall-normal turbulence intensity

Figure 8 shows for the uncontrolled and the controlled flow, the wall-normal turbulence intensity distribution $v = \sqrt{v'^2}$ on the flap normalized by U_∞ . The high level region of the uncontrolled flow (Figure 8 a)) over the first half of the flap is highly reduced in intensity (by a factor about 2) and in size. It is even more confined in the near wall region than u . In the rear part, the high level region is very similar in shape (but not in intensity) to the uncontrolled case. This raises the question of the physical origin of this region which seems to exist in both separated and reattached flow.

Reynolds shear stress

Figure 9 shows for both cases, the Reynolds shear stress distribution ($-uv = -\overline{u'v'}$) normalized by U_∞^2 . Above the flap, this stress presents a high values region which develops closer to the wall for the controlled flow (Figure 9 b)) than for the uncontrolled one (Figure 9 a)). However, the peak level for the controlled case is about four times lower. In the downstream part of the field of view, the extent of the high value region in the wall-normal direction is about two times smaller. Finally, for both cases, the high similarity between the wall normal turbulence intensity (Figure 8) and this stress should be noted.

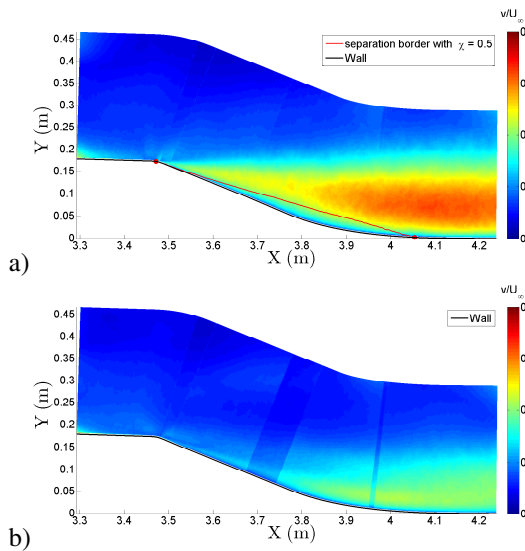


Figure 8. Wall normal turbulence intensity ($v = \sqrt{v'^2}$) on the flap for a) the uncontrolled, b) the controlled flow.

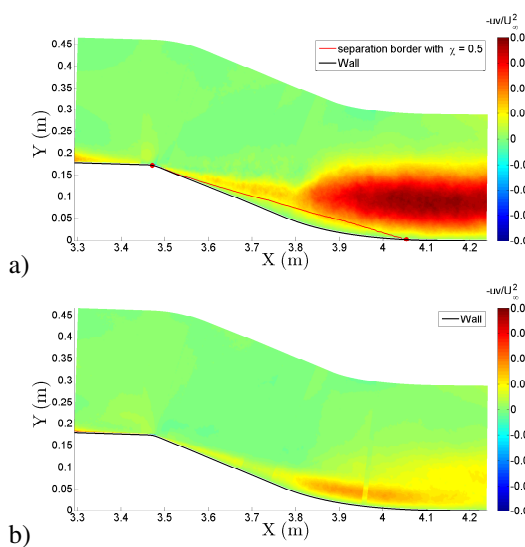


Figure 9. Reynolds shear stress ($uv = \overline{u'v'}$) on the flap for a) the uncontrolled, b) the controlled flow.

Turbulence production

Figure 10 shows the distribution of the production term $-\overline{u'v'} \frac{\partial U}{\partial y}$ of turbulent kinetic energy, normalized by U_∞^3/H_{step} for the uncontrolled (a) and controlled flow (b). Under control, the high production region near the wall upstream the corner is reduced compared to the base flow. This is coherent with the downwash region which attenuates turbulence. On the flap, this quantity gives a better insight of the physics involved. In fact, the control applied does not suppress completely the shear layer which has its origin at the corner and which is clearly visible on the base flow. It just squeezes it against the wall, reducing it in intensity. When reaching the middle of the flap (around $X = 3.8$ m) where a concave curvature appears, this shear layer suddenly expands with a second production peak closely linked to the v' fluctuations. This phenomenon is not suppressed by the control, it is just attenuated and squeezed against the wall.

Figure 11 gives the distribution of the production term

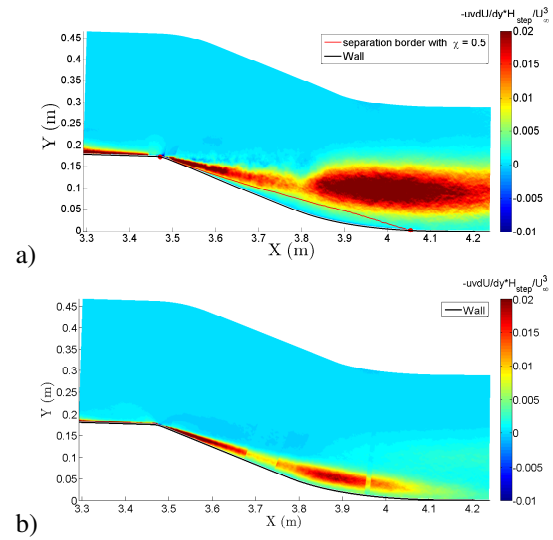


Figure 10. Production term $-\overline{u'v'} \frac{\partial U}{\partial y}$ on the flap for a) the uncontrolled, b) the controlled flow.

$-\overline{u'^2} \frac{\partial U}{\partial x}$ of turbulent kinetic energy for both cases. Here again, the high positive values region downstream the corner is also not suppressed by the actuators. Its intensity is highly reduced by the control and it is squeezed against the wall. However its streamwise extend is almost conserved. For the two others production terms accessible, the term $-\overline{u'v'} \frac{\partial V}{\partial x}$ is found negligible for both cases and the term $-\overline{v'^2} \frac{\partial V}{\partial y}$ (not shown) is found largely reduced in intensity by the control and the high levels region is squeezed against the wall as for the other production terms.

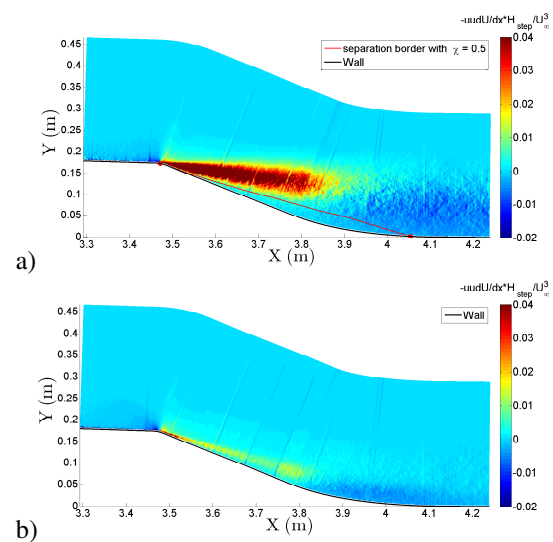


Figure 11. Production term $-\overline{u'^2} \frac{\partial U}{\partial x}$ on the flap for a) the uncontrolled, b) the controlled flow.

Concerning the production of Reynolds shear stress, for the control case, as for the uncontrolled flow, it is dominated by the term $\overline{v'^2} \frac{\partial U}{\partial y}$ (given in Figure 12), which explains the similarity observed between the Reynolds shear stress and the wall-normal turbulence intensity distribution for both cases. As for the production of turbulent kinetic energy, the high level region is also squeezed against the

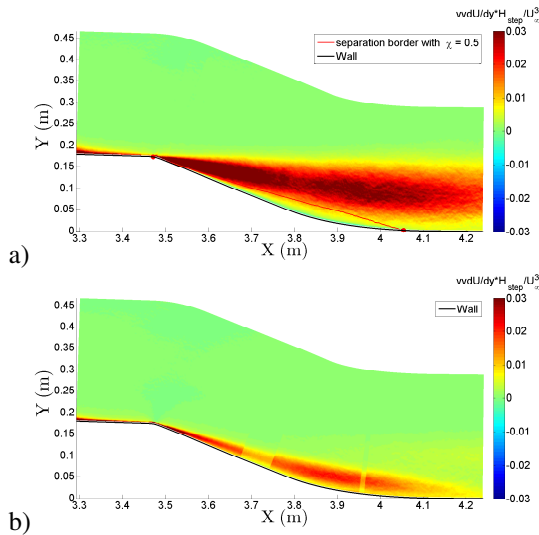


Figure 12. Production term $\overline{v^2 \frac{\partial U}{\partial y}}$ of $-\overline{u'v'}$ on the flap for a) the uncontrolled, b) the controlled flow.

wall.

The conclusion is that the control strategy used does not modify the separation physics (at least in the plane of observation). It only changes its size, intensity and location with respect to the wall. This may be due to the fact that the flow control is based on streamwise and not spanwise structures. It may also be due to the fact that the attached boundary layer on the flap is immediately submitted to an adverse pressure gradient. Two other arrangements of jets (co-rotating upstream blowing and counter-rotating downstream blowing (Cuvier (2012))) were also analysed with the same PIV measurements. The conclusions obtained are similar.

CONCLUSION

In this study, the flow reorganisation due to continuous counter-rotating jets which controls the flow separation induced by a 22° flap, was investigated through streamwise 2D2C PIV measurements at mid-span of the model.

The separation border was detected with the backflow coefficient and it results that the separation was totally suppressed by the control. The accessible Reynolds stresses with the PIV plane were presented and compared to the ones of the uncontrolled case. For the controlled flow, the three Reynolds stresses ($\overline{u^2}$, $\overline{v^2}$, $\overline{u'v'}$) exhibit a region of high levels which develops above the flap and which is similar to the high turbulence region which develops above the bubble border for the uncontrolled flow. However, its intensity is highly reduced for the controlled case and it is nearer to the wall. The same is true for the production terms which indicates that the control applied here does not suppress totally the shear layer. It just reduces its intensity and squeezes it against the wall.

The control strategy selected, based on streamwise vortices, is then probably not optimum in the sense of energetic cost as it does not act directly on the phenomena which lead to separation. Probably strategies based on spanwise vortices could be more efficient in terms of energetic cost to reach reattachment.

ACKNOWLEDGMENTS

The present research work was supported by International Campus on Safety and Intermodality in Transportation, the Nord-Pas-de-Calais Region, the European Community, the Regional Delegation for Research and Technology, the Ministry of Higher Education and Research, and the National Center for Scientific Research.

REFERENCES

- Carlier, J. & Stanislas, M. 2005 Experimental study of eddy structures in a turbulent boundary layer using particle image velocimetry. *J. Fluid Mech.* **535** (36), 143–188.
- Cuvier, C. 2012 Active control of a separated turbulent boundary layer in adverse pressure gradient. PhD thesis, Ecole Centrale de Lille.
- Cuvier, C., Foucaut, J.M., Braud, C. & Stanislas, M. 2013 Piv characterisation of a flow separation induced by a 22° flap. *TSFP8 conference, August 28-30, Poitiers, France*.
- Dengel, P. & Fernholz, H 1990 An experimental investigation of an incompressible turbulent boundary layer in the vicinity of separation. *J. Fluid Mech.* **212**, 615–636.
- Foucaut, JM, Milliat, B., Perenne, N. & Stanislas, M. 2003 Characterisation of different piv algorithm using the europiv synthetic image generator and real images from a turbulent boundary layer. In *EUROPIV2 workshop, Zaragoza, Spain* (ed. Springer).
- Godard, G. & Stanislas, M. 2006a Control of a decelerating boundary layer. part 1: Optimization of passive vortex generators. *Aerospace Science and Technology* **10** (3), 181–191.
- Godard, G. & Stanislas, M. 2006b Control of a decelerating boundary layer. part 3: Optimization of round jets vortex generators. *Aerospace Science and Technology* **10** (6), 455–464.
- Herpin, Sophie, Wong, Chong Yau, Stanislas, Michel & Soria, Julio 2008 Stereoscopic piv measurements of a turbulent boundary layer with a large spatial dynamic range. *Exp Fluids* **45**, 745–763.
- Kostas, J., Foucaut, J.-M & Stanislas, M. 2005 Application of double spiv on the near wall turbulence structure of an adverse pressure gradient turbulent boundary layer. In *6th International Symposium on PIV, Pasadena, CA*.
- Kostas, J., Foucaut, J.-M. & Stanislas, M. 2007 The flow structure produced by pulsed-jet vortex generators in a turbulent boundary layer in an adverse pressure gradient. *Flow Turbulence Combust* **78**, 331–363.
- Lin, J. C. 1999 Control of turbulent boundary layer separation using micro-vortex generators. *AIAA Paper* (99-3404).
- Lögberg, Ola 2008 Turbulent boundary layer separation and control. PhD thesis, Royal Institute of Technology KTH Mechanics, Stockholm, Sweden.
- Lögberg, Ola, Angele, Kristian & Alfredsson, Henrik 2010 On the robustness of separation control by streamwise vortices. *European Journal of Mechanics B/Fluids* **29**, 9–17.
- Selby, G. V., Lin, J. C. & Howard, F. G. 1992 Control of low-speed turbulent separated flow using jet vortex generators. *Experiments in Fluids* **12**, 394–400.
- Simpson, R. L. 1989 Turbulent boundary layer separation. *Ann. Rev. Fluid Mech.* **21**, 205–234.